Journal of Solid State Chemistry 182 (2009) 1304–1311

Contents lists available at ScienceDirect

Journal of Solid State Chemistry

journal homepage: www.elsevier.com/locate/jssc

Structural changes accompanying negative thermal expansion in $Zr_2(MoO_4)(PO_4)_2$

Mehmet Cetinkol [a], Angus P. Wilkinson [a,*], Peter L. Lee [b]

[a] School of Chemistry and Biochemistry, Georgia Institute of Technology, Atlanta, GA 30332-0400, USA
[b] XOR, Advanced Photon Source, Argonne National Laboratory, Argonne, IL 60439, USA

ARTICLE INFO

Article history:
Received 1 July 2008
Received in revised form
3 February 2009
Accepted 27 February 2009
Available online 6 March 2009

Keywords:
Thermal expansion
Crystal structure

ABSTRACT

$Zr_2(MoO_4)(PO_4)_2$ is orthorhombic ($Sc_2W_3O_{12}$ structure) from 9 to at least 400 K, and shows anisotropic volume negative thermal expansion ($\alpha_a = -8.35(4)\times10^{-6}K^{-1}$; $\alpha_b = 3.25(3)\times10^{-6}K^{-1}$; $\alpha_c = -8.27(5)\times10^{-6}K^{-1}$ in the range 122–400 K) similar in magnitude to $A_2M_3O_{12}$ (M—Mo or W) with large A^{3+}. The contraction on heating is associated with a pattern of Zr–O–Mo/P bond angle changes that is somewhat similar, but not the same as that for $Sc_2W_3O_{12}$. On heating, the most pronounced reductions in the separation between the crystallographic positions of neighboring Zr and P are not associated with significant reductions in the corresponding Zr–O–P crystallographic bond angles, in contrast to what was seen for $Sc_2W_3O_{12}$.

1. Introduction

Negative thermal expansion (NTE) materials continue to attract attention due to intrinsic interest in this phenomenon and their potential for application in controlled thermal expansion composites and other areas. Many compositions are known to form with structures related to that of orthorhombic $Sc_2W_3O_{12}$ [1–4]. They typically display anisotropic volume NTE while orthorhombic, but are susceptible to symmetry lowering phase transitions [5], with a concomitant loss of NTE, on cooling or modest compression [6–9]. The $Sc_2W_3O_{12}$ framework is amenable to a wide range of substitutions beyond the simple replacement of Sc^{3+} with other trivalent ions; for example, materials such as $A_2(MO_4)(PO_4)_2$ (A—Zr or Hf; M—W or Mo) [10–13], $(HfMg)(WO_4)_3$ [14–17], and $Zr_2(SO_4)(PO_4)_2$ [18] have been reported to have related structures. The wide range of possible substitutions allows for tuning of both thermal and high-pressure behavior. The use of $A_2(MO_4)(PO_4)_2$ (A—Zr or Hf; M—W or Mo) in controlled thermal expansion applications is covered by several patents including [19,20]. As a prelude to exploring the behavior of $Zr_2(MoO_4)(PO_4)_2$ under pressure, we have examined the expansion of this compound and the structural changes underlying its behavior by a combination of neutron, high-resolution synchrotron X-ray and variable temperature medium resolution synchrotron powder diffraction.

The structural changes underlying NTE in $A_2M_3O_{12}$ type materials have previously been examined in some detail for $Sc_2W_3O_{12}$ [2,3], $Sc_2Mo_3O_{12}$ [6], $Y_2W_3O_{12}$ and $Al_2W_3O_{12}$ [21]. It has been proposed that the NTE arises from a cooperative tilting of relatively rigid polyhedra driven by the anharmonic nature of the transverse vibrations of bridging oxygen atoms [2]. This decreases some M–O–M' angles, leading to a decrease in the corresponding M–M' distances and an overall contraction. The structural changes associated with NTE in $Zr_2(MoO_4)(PO_4)_2$ are compared and contrasted with those previously reported for $Sc_2W_3O_{12}$ [2].

2. Experimental

2.1. Sample preparation

Two separate batches of $Zr_2(MoO_4)(PO_4)_2$ were prepared using stoichiometric amounts of ZrO_2 (Alfa Aesar, 99.7%), $NH_4H_2PO_4$ (J.T. Baker, 99.2%) and 20% excess MoO_3 (J.T. Baker, 99.8%). The starting compounds were ground together in an agate mortar, heated in an alumina crucible for 4 h at 600 °C, 2 h at 900 °C and, finally, 30 min at 1000 °C. This treatment was followed by grinding and heating for another 5 h at 900 °C resulting in off-white powders. Laboratory powder diffraction data, obtained using a Scintag X1 diffractometer equipped with a copper tube and a Peltier cooled solid-state detector, indicated that the batch used for the variable temperature X-ray study was single phase. The second batch was used for neutron diffraction and the high-resolution X-ray experiments.

2.2. Synchrotron high-resolution X-ray diffraction study

High-resolution synchrotron X-ray powder diffraction data for $Zr_2(MoO_4)(PO_4)_2$ were obtained at room temperature using the

* Corresponding author. Fax: +1 404 894 7452.
E-mail address: angus.wilkinson@chemistry.gatech.edu (A.P. Wilkinson).

0022-4596/$ - see front matter © 2009 Elsevier Inc. All rights reserved.
doi:10.1016/j.jssc.2009.02.029

11-BM-B beamline of the Advanced Photon Source, Argonne National Laboratory [22]. A Si(111) double crystal monochromator provided 0.4017 Å X-rays from a bending magnet. A triple axis geometry was employed using 12 scintillation detectors each with its own Si(111) analyzer crystal [23]. The sample was contained in a 0.8 mm diameter capillary and data collected over the range 2°–36° 2θ in 0.001° steps. A relatively short X-ray wavelength was employed, as is typical for this beamline, as this facilitates the use of quite large diameter capillary samples while keeping systematic errors due to phenomena such as absorption and poor sampling statistics under good control. With a triple-axis instrument geometry and perfect crystal analyzers, the use of short wavelength X-rays does not lead to a dramatic degradation of angular resolution in the powder diffraction data, as the angular acceptance of the analyzer crystals decreases as the X-ray wavelength is reduced.

The program suite GSAS [24] with the EXPGUI [25] graphical interface was used for the Rietveld [26] analysis of this powder X-ray diffraction data. Initial analysis showed the presence of MoO_3 (<1% by weight) and ZrO_2 (~2% by weight) as trace impurities. The final Rietveld refinement included these impurities (fit shown in Fig. 1). Only the lattice constants, two Lorentzian profile coefficients and scale factors were refined for the impurities. The $Zr_2(WO_4)(PO_4)_2$ structure reported by Evans [11] (*Pnca*) was used as a starting model. The background was fitted with a 15 term Chebyshev polynomial. Peak profiles were modeled using a pseudo-Voigt function. Independent isotropic atomic displacement parameters were used for all atoms. The effects of absorption were modeled within GSAS assuming a 30% packing density for the capillary and a computed linear absorption coefficient of 13.12 cm^{-1}. Some of the peaks for the main phase showed an asymmetry (see Fig. 2) that was attributed to the presence of a narrow range of lattice constants, where the distribution of lattice constants was not symmetrical. Similar issues were reported by Evans for $Zr_2(WO_4)(PO_4)_2$ [11]. This unusual peak shape was modeled by using two $Zr_2(MoO_4)(PO_4)_2$ "phases" in the refinement that were constrained to be structurally identical to one another, but allowed to have different lattice constants and peak shapes. Our use of this model should not be taken to imply that we believe there are two distinct phases of $Zr_2(MoO_4)(PO_4)_2$ in the sample. The structural parameters resulting from this analysis are summarized in Table 1.

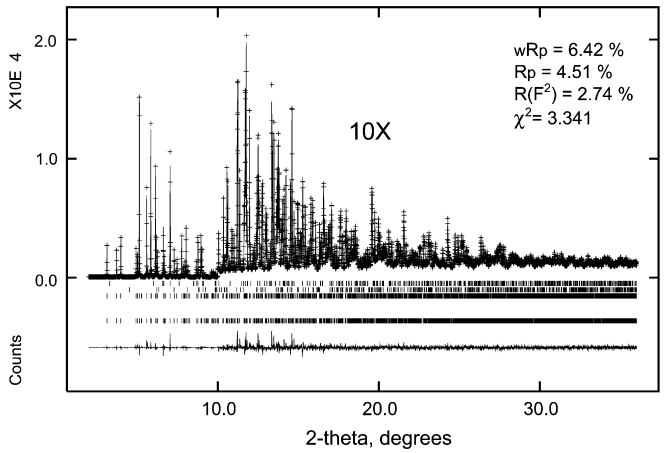

Fig. 1. Rietveld fit to the 300 K high-resolution synchrotron data for $Zr_2(MoO_4)(PO_4)_2$. Observed (+), calculated (−), and difference (bottom trace) powder diffraction patterns are shown along with tag marks indicating the Bragg peak positions for trace MoO_3 (top) and ZrO_2 (second from top) impurities and the two "phases" of $Zr_2(MoO_4)(PO_4)_2$ (lower set of marks).

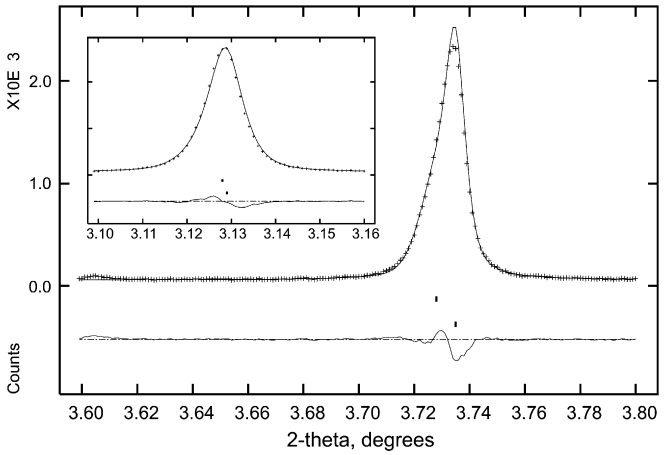

Fig. 2. Examples of peak asymmetry in the 300 K high-resolution synchrotron data for $Zr_2(MoO_4)(PO_4)_2$.

Table 1
Structural parameters for $Zr_2(MoO_4)(PO_4)_2$ at 300 K determined by Rietveld analysis of the synchrotron high-resolution X-ray data.

Atom	*x*	*y*	*z*	U_{iso}*100
Zr1	0.04744(3)	0.37004(2)	0.22606(3)	0.38(1)
Mo1	0.25	0	0.03890(4)	0.45(1)
P1	0.60513(9)	0.85615(8)	0.3830(1)	0.25(3)
O1	0.9294(2)	0.3492(2)	0.0447(2)	0.56(6)
O2	0.8697(2)	0.4275(2)	0.3491(2)	1.35(7)
O3	−0.0044(2)	0.2196(2)	0.3005(2)	0.36(6)
O4	0.1565(2)	0.4074(2)	0.4271(2)	1.08(7)
O5	0.0811(2)	0.5282(2)	0.1715(2)	0.47(6)
O6	0.2397(2)	0.3242(1)	0.1418(2)	0.55(6)

Lattice constants for the two "phases" used to model the complex peak shape were $a = 9.33504(3)$ Å, $b = 12.32430(4)$ Å, $c = 9.16613(3)$ Å for the main component, and $a = 9.32849(8)$ Å, $b = 12.3473(1)$ Å, $c = 9.16300(7)$ Å for the minor component.

2.3. Variable temperature powder neutron diffraction

Neutron powder diffraction data were collected using the 32 detector BT-1 instrument at the NIST Center for Neutron Research reactor, NBSR. A Ge(311) monochromator with a 75° take-off angle, $\lambda = 2.0787$ Å, and in-pile collimation of 15 min of arc were used. The instrument is described in the NCNR website (http://ncnr.nist.gov). The sample was sealed in a 15.6 mm diameter vanadium can inside a dry He-filled glovebox. Data were collected over the range of 3°–165° 2θ, with a step size of 0.05°, at both 298 and 9 K, using a closed cycle refrigerator. The program suite GSAS [24] with the EXPGUI [25] graphical interface was used to perform Rietveld [26] analyses. The background was fitted with a Chebyshev polynomial function with 20 coefficients. The Bragg peak profiles were modeled using a pseudo-Voigt function. Independent isotropic atomic displacement parameters were used for all atoms. The Rietveld fit to the 9 K data is shown in Fig. 3. The structural parameters resulting from these analyses are provided in the Supplementary material.

2.4. Variable temperature powder X-ray diffraction

17.53 keV ($\lambda = 0.70736$ Å) X-rays were used at the APS beamline 1-BM-C, Argonne National Laboratory, in combination with a MAR-345 imaging plate detector, to record 2D diffraction patterns for $Zr_2(MoO_4)(PO_4)_2$ in a 0.7 mm diameter glass capillary. This

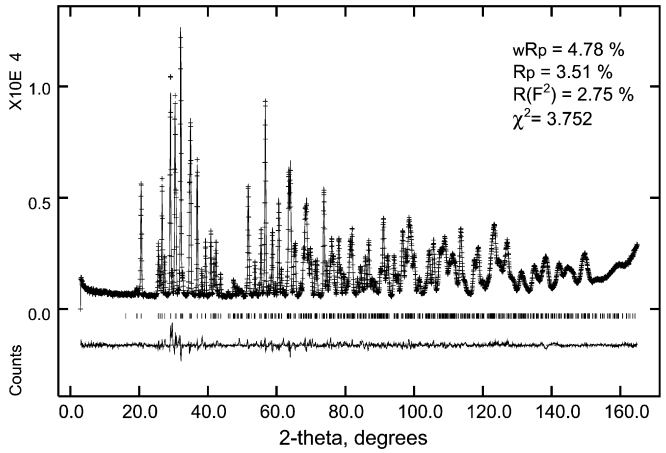

Fig. 3. Rietveld fit to the 9 K neutron diffraction data for $Zr_2(MoO_4)(PO_4)_2$. Observed (+), calculated (−), and difference (bottom trace) powder diffraction patterns are shown along with tag marks indicating the Bragg peak positions for $Zr_2(MoO_4)(PO_4)_2$.

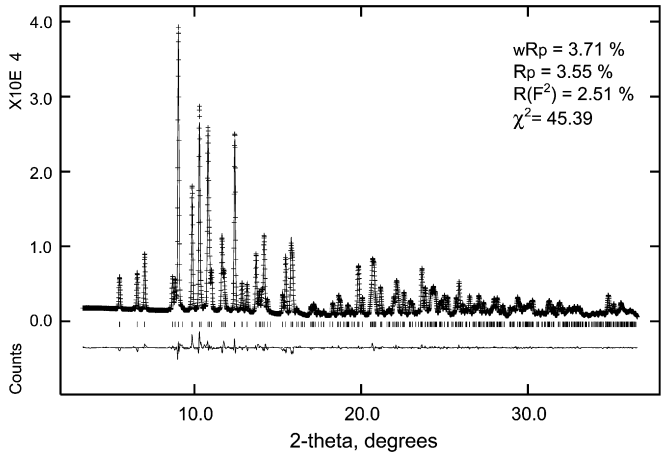

Fig. 4. Rietveld fit to the image plate X-ray data for $Zr_2(MoO_4)(PO_4)_2$ recorded at approximately 300 K. Observed (+), calculated (−), and difference (bottom trace) powder diffraction patterns are shown along with tag marks indicating the Bragg peak positions for $Zr_2(MoO_4)(PO_4)_2$.

wavelength, which is just below both the Zr and Mo*K*-edges (~18 and ~20 keV, respectively), was chosen to minimize sample absorption while remaining in the usable energy range of the beam line. The detector was vertically offset to increase the 2θ range, such that the X-ray beam was centered close to the bottom of the imaging plate. Eighty-six diffraction patterns were recorded (2.5 s exposures plus readout time) while continuously cooling the sample from 400 to 85 K at 120 K h^{-1} using an Oxford Cryosystem's Cryostream 700. Powder diffraction data were also collected for a 1:3 mixture of silicon and alpha alumina under identical conditions. The measured lattice constants for these standards were compared with those expected based on their known thermal expansion [27,28] to verify the temperature calibration. The raw 2D images were processed using Fit2D [29]. The sample to detector distance (ca. 340 mm) and tilt of the image plate relative to the beam were refined using data from a LaB_6 calibrant. Analysis of the integrated diffraction patterns was undertaken using the GSAS suite and the SeqGSAS utility was used to process all of the patterns sequentially. The Rietveld analyses were done assuming single phase $Zr_2(MoO_4)(PO_4)_2$. The background was fitted with a Chebyshev polynomial function with 20 coefficients. The Bragg peak profiles were modeled using a pseudo-Voigt function. Isotropic atomic displacement parameters were used.

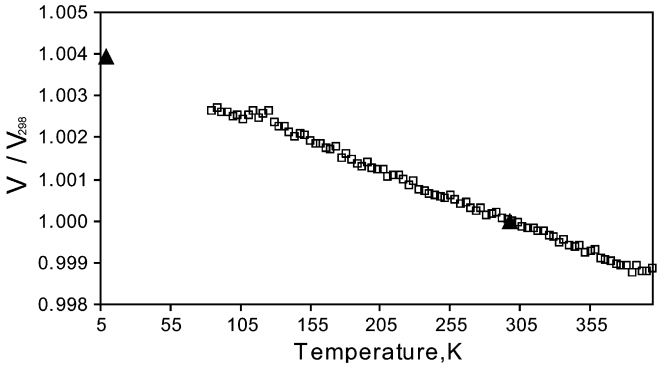

Fig. 5. Normalized unit cell volume as a function of temperature derived from the image plate (open squares) and neutron data (closed triangles).

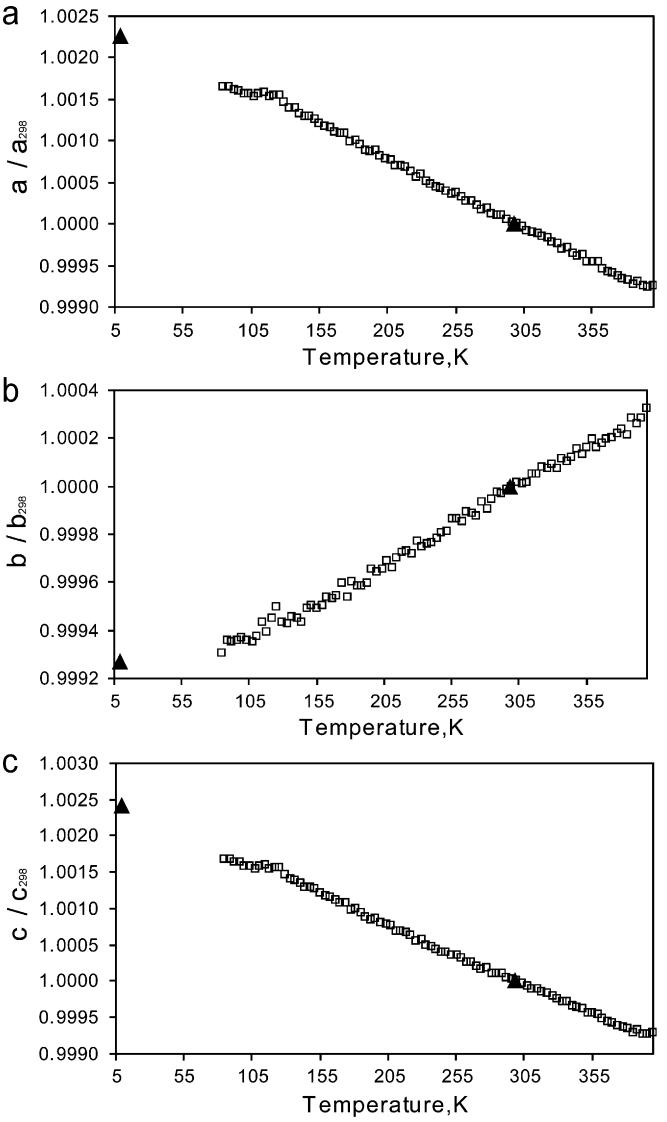

Fig. 6. Normalized lattice constants as a function of temperature derived from the image plate (open squares) and neutron data (closed triangles).

Absorption corrections for image plate data with cylindrical samples are more complex to implement than those used with cylindrical samples on a diffractometer, because the correction is not purely a function of 2θ (it varies around each Debye ring). As

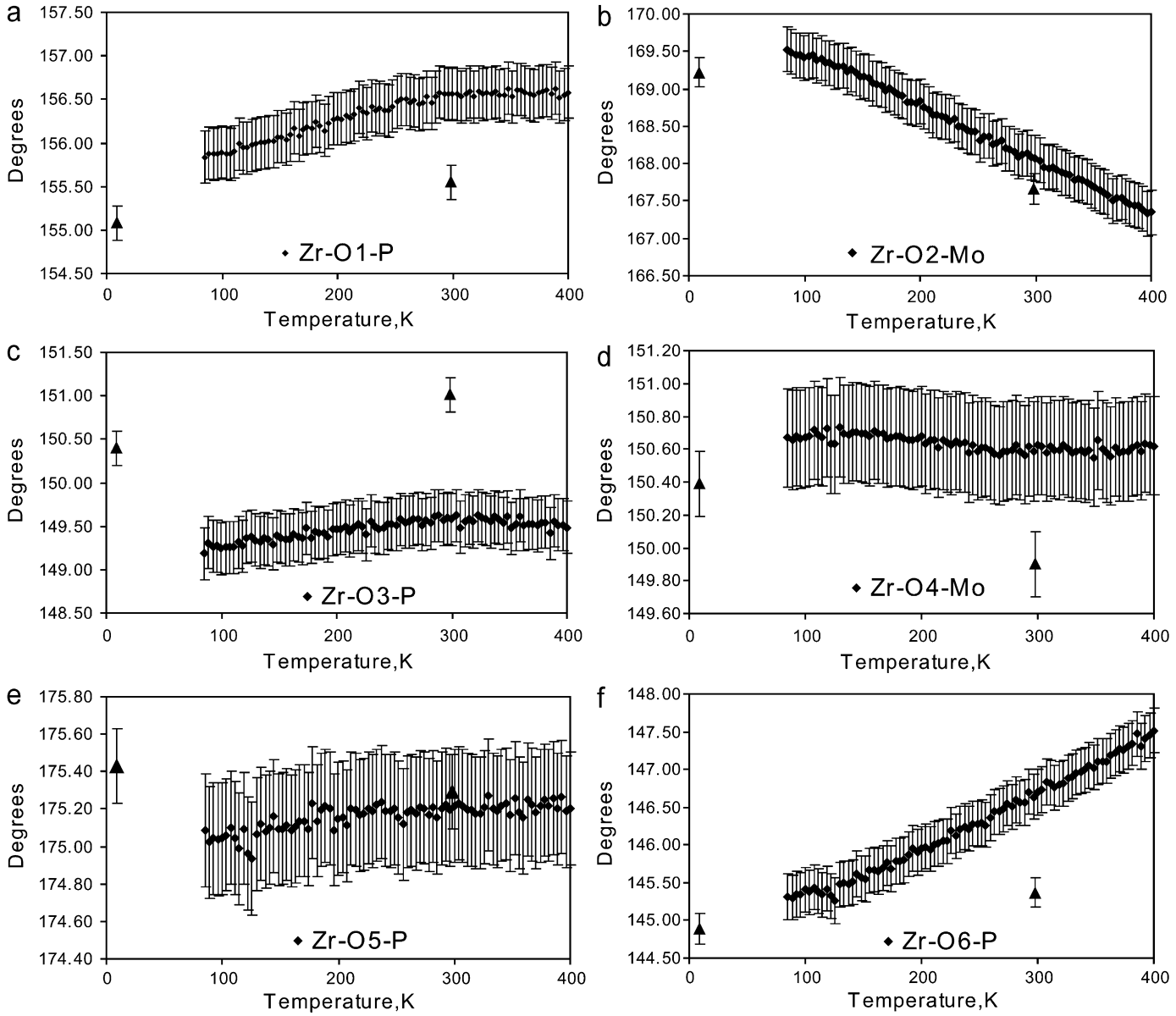

Fig. 7. Zr–O–Mo/P angles, as a function of temperature, from the image plate X-ray (diamonds) and neutron (triangles) diffraction data. Error bars represent typical Rietveld e.s.d.s.

μR for the sample was low (estimated as ~0.35), and the correction difficult to implement, we elected not to apply an absorption correction to our 2D data.

The Rietveld fit to the 300 K data is shown in Fig. 4. The structural parameters resulting from the analysis of these data are available in the supplementary material. The variation of the unit cell volume and the cell constants with temperature are shown in Figs. 5 and 6, respectively. Selected geometrical parameters, as a function of temperature, are shown in Figs. 7–9.

2.5. Joint refinement using ambient temperature neutron and X-ray data

A combined analysis of the 300 K high-resolution X-ray data and 298 K neutron data was carried out to explore the possibility of mixed Mo/P site occupancy and/or vacancies on the tetrahedral sites.

3. Results and discussion

3.1. Room temperature crystal structure

Rietveld analysis of the room temperature high-resolution synchrotron data for $Zr_2(MoO_4)(PO_4)_2$ provided no evidence for symmetry lower than *Pnca*. This is consistent with prior work on the analogous tungstate [11]. The observed asymmetric peaks shapes (Fig. 2) for some types of reflection are indicative of an asymmetric distribution of lattice constants within the sample, not symmetry lowering. Our fit to asymmetric peak shapes made use of two $Zr_2(WO_4)(PO_4)_2$ "phases" that were constrained to be structurally identical but had independently refineable lattice constants and scale factors. This is a useful simplification, but a continuous distribution of lattice constants amongst separate coherent diffracting domains is expected. The predominant difference between the two "phases" used in the model was that the *b* lattice constant for the minor "phase" was

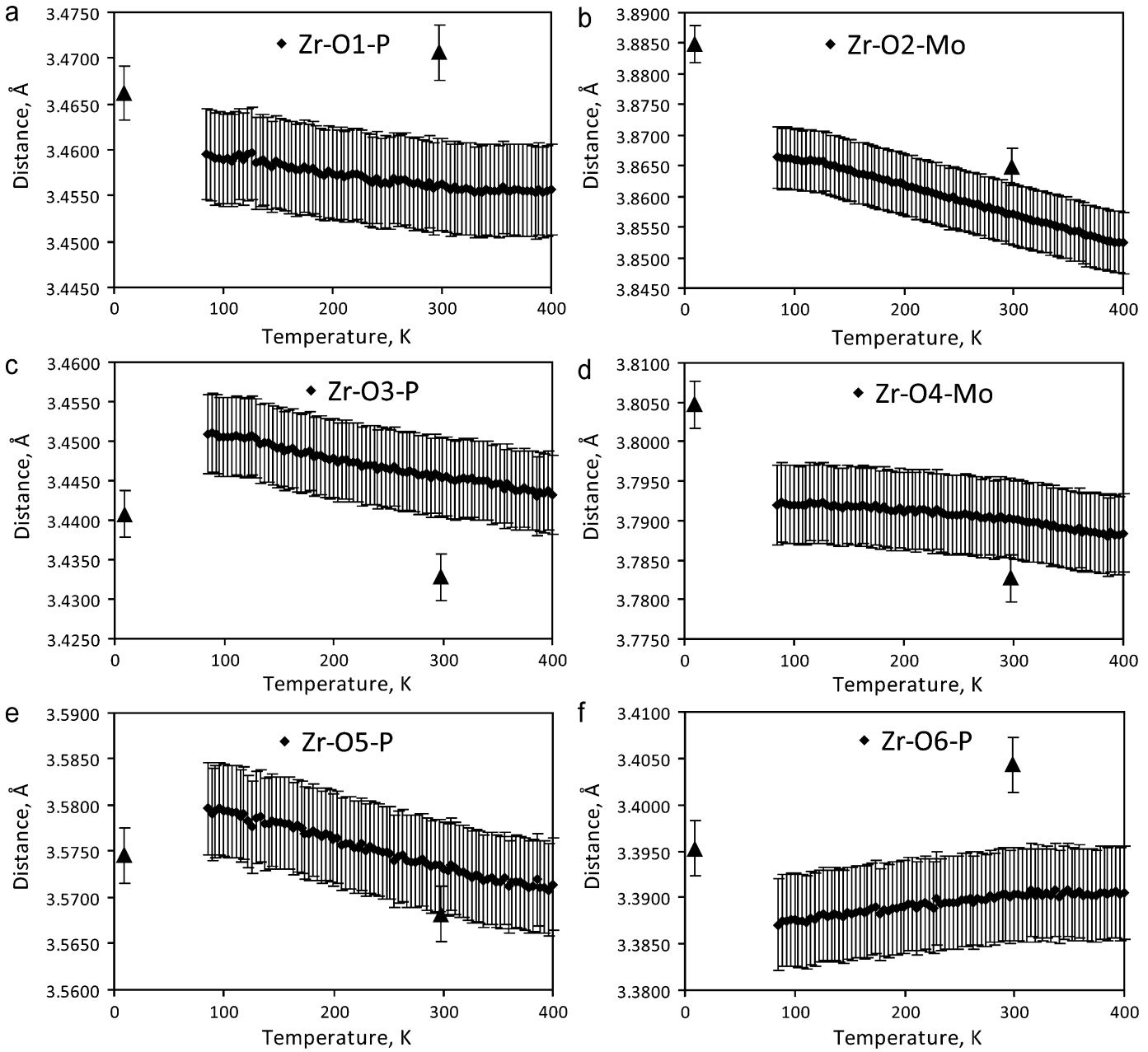

Fig. 8. Individual nonbonding Zr–O–Mo/P distances as a function of temperature, from the image plate X-ray (diamonds) and neutron (triangles) diffraction data. Error bars represent typical Rietveld e.s.d.s.

1.002 times that of the major "phase" (Table 1). The other lattice constants for the two "phases" differed by much less than this. This distribution of lattice constants is presumably associated with some type of defect in the sample that predominantly affects the *b* lattice constant. Using a combined analysis of the high-resolution X-ray data and 298 K neutron data, we explored the possibility of vacancies and/or Mo/P substitution on the tetrahedral sites of the structure to see if this could be a possible origin of the lattice constant variation. The combined refinement was fully consistent with complete occupancy of the tetrahedral sites with a single species (Mo or P).

3.2. Is there a structural phase transition at low temperature?

Many compounds with a $Sc_2W_3O_{12}$ type structure show a monoclinic to orthorhombic phase transition on heating from very low temperatures, although $Sc_2W_3O_{12}$ is orthorhombic at all temperatures that have been examined [2,3]. For example, $Sc_2Mo_3O_{12}$ goes from $P2_1/a$ to *Pnca* at 178 K on heating [6]. Analysis of the neutron diffraction data for $Zr_2(MoO_4)(PO_4)_2$ recorded at 9 and 298 K showed no evidence of a phase transition on cooling from room temperature. Both data sets could be modeled very well in space group *Pnca*.

3.3. Thermal expansion in $Zr_2(MoO_4)(PO_4)_2$

The normalized unit cell volume and lattice constants for $Zr_2(MoO_4)(PO_4)_2$, as determined by Rietveld analysis of the data from the variable temperature X-ray experiment (cooling from 400 to 85 K) and neutron experiments (298 and 9 K), are shown in Figs. 5 and 6, respectively. The minor anomalies in the X-ray derived values between 85 and ~125 K are believed to be experimental artifacts associated with the cryostream cooling

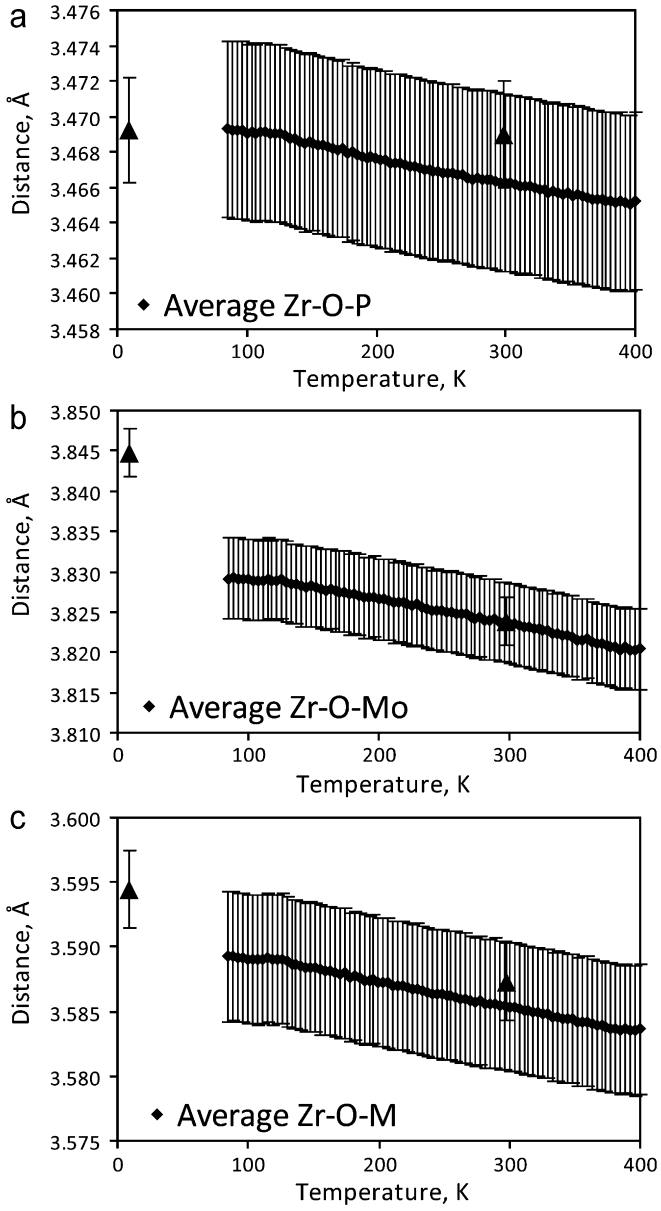

Fig. 9. Average nonbonding Zr–O–Mo/P distances, as a function of temperature, from the image plate X-ray (diamonds) and neutron (triangles) diffraction data. Error bars represent typical Rietveld e.s.d.s.

system. Thermal expansion coefficients estimated from the neutron derived lattice constants are in good agreement with those from the variable temperature X-ray study, lending further confidence to the temperature calibration in the X-ray experiment (see Table 2). There is a continuous expansion of the unit cell volume on cooling, associated with a volume thermal expansion coefficient, α_v, of $-13.4(1)\times10^{-6}\,K^{-1}$. The expansion of $Zr_2(MoO_4)(PO_4)_2$ is anisotropic, such that the b axis expands with increasing temperature while the a and c axes contract ($\alpha_a=-8.35(4)\times10^{-6}\,K^{-1}$; $\alpha_b=3.25(3)\times10^{-6}\,K^{-1}$; $\alpha_c=-8.27(5)\times10^{-6}\,K^{-1}$, obtained from straight line fits to ln(L) versus T between 400 and 122 K). The coefficients of thermal expansion for $Zr_2(MoO_4)(PO_4)_2$ are compared with those for related compounds in Table 2. The anisotropy of the expansion for $Zr_2(MoO_4)(PO_4)_2$ is similar to that for the listed $A_2^{3+}(MO_4)_3$. However, for $A_2^{3+}(MO_4)_3$ (M—W or Mo), α_v becomes increasingly negative as the size of the M^{3+} ion and unit cell volume increase, but $Zr_2(MoO_4)(PO_4)_2$ does not fit this unit cell volume and expansion coefficient trend. It has a unit cell volume similar to that of $Al_2(WO_4)_3$ [21], with α_v closer to that of $A_2^{3+}(MO_4)_3$ with much larger unit cell volumes.

3.4. Structural changes associated with thermal expansion

As the changes in unit cell dimensions with temperature (Figs. 5 and 6) must be a result of structural changes, we examined the behavior of the crystal structure as a function of temperature. The synchrotron image plate experiment spanned a significant temperature range (85–400 K) and included many temperature points. While the d-spacing range for these patterns ($d_{min}\sim1.13$ Å) is less than that typically used for high-quality structure refinements, a comparison of the bond lengths and angles derived from the high-resolution synchrotron data, neutron data and image plate data all at ~300 K gives confidence that the coordinates obtained from the Rietveld analysis of the image plate data are reliable (Table 3); the geometrical parameters derived from all three measurements are precise and in very good agreement with one another. Graphs showing the temperature dependence of selected distances and angles for the $Zr_2(MoO_4)(PO_4)_2$ structure are shown in Figs. 7–9. The scatter in these graphs is low, enabling an examination of structural trends with temperature.

$Zr_2(MoO_4)(PO_4)_2$ consists of corner sharing ZrO_6 octahedra and MoO_4/PO_4 tetrahedra with only small distortions from ideal geometry (see Table 3 and Supplementary material, Table S4). The ZrO_6 octahedron is similar in size to the ScO_6 octahedron in $Sc_2W_3O_{12}$, but PO_4 is significantly smaller than MoO_4/WO_4, leading to a smaller unit cell volume for $Zr_2(MoO_4)(PO_4)_2$ than $Sc_2W_3O_{12}$ (Table 2). Zr–O, Mo–O and P–O bonded distances calculated from the crystallographic atomic positions only vary slightly with temperature as would be expected for strong bonds (see Supplementary material, Figs. S1, S2 and S3). The slight decrease in some of these distances on heating can be ascribed to the correlated (thermal) vibrational motion of the bonded pairs of atoms rather than any real reduction in instantaneous bond length [2]. Earlier work on the related compounds $Sc_2(WO_4)_3$ [2], $Sc_2(MoO_4)_3$ [6], and $Y_2(WO_4)_3$ [21] suggested that the NTE behavior in this type of material was associated with the transverse thermal vibration of bridging O atoms and related changes in A–O–M bond angles. Fig. 7 shows the variation in six different Zr–O–Mo/P angles for $Zr_2(MoO_4)(PO_4)_2$. Evans et al. [2] reported that for $Sc_2W_3O_{12}$, the two largest A–O–M angles (Sc–O2–W and Sc–O5–W) decreased significantly on heating from 10 to 450 K, but the smallest angles (Sc–O6–W, Sc–O4–W) increased and the intermediate angles did not show a significant trend with temperature. They also described how these changes led to the observed thermal expansion characteristics of the material. A–O–M angles from a variable temperature neutron diffraction study of $Sc_2W_3O_{12}$, using three different isotopically labeled samples, showed the same overall trend [3]. Somewhat similar behavior is seen for $Zr_2(MoO_4)(PO_4)_2$. However, the largest Zr–O–Mo/P angle, Zr–O5–P, is essentially independent of temperature. Only the Zr–O2–Mo angle decreases strongly on heating. The smallest angle Zr–O6–P increases strongly on heating, similar to Sc–O6–W, but there is no strong trend in Zr–O4–Mo with temperature. The other two angles Zr–O1–P and Zr–O3–P show a slight increase on heating before leveling out at the highest temperatures examined. Changes in non-bonded Zr–Mo/P separations, calculated from crystallographic atomic positions, as a function of temperature, are shown in Fig. 8. As would be expected from the temperature dependences of the Zr–O2–Mo and Zr–O6–P angles in a material with almost rigid Zr–O, P–O and Mo–O links, the Zr–Mo distances for Zr–O2–Mo decreases quite strongly on heating and the Zr–P distance for Zr–O6–P increase on

Table 2
Coefficients of thermal expansion for $Zr_2(MoO_4)(PO_4)_2$ and its relatives.

Compound	Radii M^{3+}/M^{4+} (pm)[a]	α_a (ppm K^{-1})	α_b (ppm K^{-1})	α_c (ppm K^{-1})	Anisotropy[b]	$V/Å^3$	α_v (ppm K^{-1})	T range (K)	Reference
$Al_2(WO_4)_3$	53.5	−1.31	5.94	−0.099	7.25	1042	4.51	273–1073	[21]
$Sc_2(WO_4)_3$	74.5	−6.3	7.5	−5.5	13.8	1234	−6.5	50–450	[2]
$Sc_2(MoO_4)_3$	74.5	−8.41	10.82	−8.73	19.55	1220	−6.3	200–300	[6]
$Lu_2(WO_4)_3$	86.1	−9.9	−2.2	−8.3	7.7	1345	−20.4	400–900	[30]
$Y_2(WO_4)_3$	90	−10.35	−3.06	−7.62	7.29	1401	−20.9	273–1073	[21]
$Zr_2(WO_4)(PO_4)_2$	72						−9	50–450	[4]
		−7.3	1.4	−8.4	9.8	1055	−14.2	60–298	[31]
$Zr_2(MoO_4)(PO_4)_2$	72	−8.35	3.25	−8.27	11.6	1055	−13.4	122–400	Current
		−7.82	2.53	−8.34	10.87	1056	−13.6	9–298	Current

[a] Ionic radii for six coordinate cations from Shannon 1976 [32].
[b] Anisotropy $= \alpha_{l\,max} - \alpha_{l\,min}$.

Table 3
Selected bond distances (Å) and angles (deg).

	O1	O2	O3	O4	O5	O6
Zr1	2.011(2)	2.127(2)	2.035(2)	2.155(2)	2.037(2)	2.034(2)
	2.019(5)	2.153(5)	2.056(4)	2.170(5)	2.046(5)	2.039(5)
	2.022(3)	2.145(3)	2.034(3)	2.173(3)	2.051(3)	2.018(3)
Mo1		1.761(2)		1.765(2)		
		1.725(5)		1.746(6)		
		1.749(3)		1.744(4)		
P1	1.519(2)		1.525(2)		1.527(2)	1.518(2)
	1.509(5)		1.511(5)		1.530(6)	1.496(6)
	1.530(4)		1.513(3)		1.519(4)	1.535(4)
Zr–O–Mo		166.6(1)		150.3(1)		
		168.1(3)		150.6(3)		
		167.6(2)		150.0(2)		
Zr–O–P	156.3(1)		150.5(1)		175.1(1)	145.8(1)
	156.6(3)		149.6(3)		175.2(3)	146.7(3)
	155.3(2)		151.0(2)		175.0(2)	145.4(2)

High-resolution X-ray 300 K (top row); variable T X-ray 300 K (middle row); neutron 298 K (bottom row).

heating. However, the Zr–P separations for both Zr–O3–P and Zr–O5–P decrease significantly on heating, even though the crystallographic bond angles for these links are essentially temperature independent. While this is different from the behavior seen in $Sc_2W_3O_{12}$, where the larger Sc–O–W bond angles decreased on heating leading to an overall thermal contraction, our observations are still consistent with NTE arising from the correlated vibrational motion of framework atoms, as there is no particular reason why such motion has to lead to a decrease in bond angle even if the angle is initially large.

In $Zr_2(MoO_4)(PO_4)_2$, the separations between the average positions of neighboring Zr and P/Mo atoms decreases (Fig. 9) leading to volume NTE. While the expansion coefficients for the average neighboring Zr–P, Zr–Mo and Zr–Mo/P separations (−4.1, −7.9 and $-5.5\times10^{-6}\,K^{-1}$, respectively) are not required to be in agreement with those determined directly from the lattice constants, they compare quite well to the average linear expansion coefficient for the material determined from its lattice constants ($-4.5\times10^{-6}\,K^{-1}$).

4. Conclusions

$Zr_2(MoO_4)(PO_4)_2$, unlike most tungstates and molybdates in the $Sc_2W_3O_{12}$ structural family maintains an orthorhombic structure showing NTE down to very low temperatures (at least 9 K). The compound displays anisotropic volume NTE, with an average linear expansion coefficient ($-4.5\times10^{-6}\,K^{-1}$) similar to that of $A_2^{3+}(MO_4)_3$ (M—Mo or W) that have significantly larger unit cell volumes than the molybdate phosphate. The structural changes (variation of M–O–M' bond angles) that accompany NTE in $Zr_2(MoO_4)(PO_4)_2$ are not identical to those previously described for $Sc_2W_3O_{12}$. While the reduction in the Zr–(O2)–Mo separation on heating is associated with a decrease in the Zr–(O2)–Mo bond angle, some Zr–P non-bonded nearest neighbor separations decrease on heating, even though the corresponding Zr–O–P bond angles do not decrease.

Acknowledgments

APW is grateful for support under National Science Foundation Grants DMR-0203342 and DMR-0605671. We acknowledge the support of the National Institute of Standards and Technology, US Department of Commerce, in providing the neutron research facilities used in this work. We are grateful for technical assistance, with the collection of the neutron powder diffraction data, from Sarah Poulton at NCNR, NIST. Use of the Advanced Photon Source was supported by the US Department of Energy, Office of Science, Office of Basic Energy Sciences, under Contract no. DE-AC02-06CH11357.

Appendix A. Supplementary material

Supplementary data associated with this article can be found in the online version at doi:10.1016/j.jssc.2009.02.029.

References

[1] S.C. Abrahams, J.L. Bernstein, J. Chem. Phys. 45 (1966) 2745–2752.
[2] J.S.O. Evans, T.A. Mary, A.W. Sleight, J. Solid State Chem. 137 (1998) 148–160.
[3] M.T. Weller, P. Henry, C.C. Wilson, J. Phys. Chem. B 104 (2000) 12224–12229.
[4] J.S.O. Evans, T.A. Mary, A.W. Sleight, J. Solid State Chem. 133 (1997) 580–583.
[5] A.W. Sleight, L.H. Brixner, J. Solid State Chem. 7 (1973) 172–174.
[6] J.S.O. Evans, T.A. Mary, Int. J. Inorg. Mater. 2 (2000) 143–151.
[7] T. Varga, A.P. Wilkinson, C. Lind, W.A. Bassett, C.-S. Zha, Phys. Rev. B 71 (2005) 214106-1–214106-8.
[8] T. Varga, A.P. Wilkinson, C. Lind, W.A. Bassett, C.-S. Zha, J. Phys.: Condens. Matter 17 (2005) 4271–4283.
[9] T. Varga, A.P. Wilkinson, J.D. Jorgensen, S. Short, Solid State Sci. 8 (2006) 289–295.
[10] A.N. Tsvigunov, V.P. Sirotinkin, Russ. J. Inorg. Chem. 35 (1990) 1740.
[11] J.S.O. Evans, T.A. Mary, A.W. Sleight, J. Solid State Chem. 120 (1995) 101–104.
[12] C.A. Martinek, F.A. Hummel, J. Am. Ceram. Soc. 53 (1970) 159–161.
[13] V.P. Sirotinkin, A.N. Tsvigunov, Russ. J. Inorg. Chem. 39 (1994) 735–736.
[14] A.M. Gindhart, C. Lind, M. Green, J. Mater. Res. 23 (2008) 210–213.
[15] T. Suzuki, A. Omote, J. Am. Ceram. Soc. 87 (2004) 1365–1367.
[16] T. Suzuki, A. Omote, J. Ceram. Soc. Jpn. 114 (2006) 833–837.
[17] T. Suzuki, A. Omote, J. Am. Ceram. Soc. 89 (2006) 691–693.
[18] Y. Piffard, A. Verbaere, M. Kinoshita, J. Solid State Chem. 71 (1987) 121–130.
[19] A.W. Sleight, M.A. Thundathil, J.S.O. Evans, Patent US 5 919 720, 1999.

[20] G.A. Merkel, Patent US 6 187 700 B1, 2001.
[21] D.A. Woodcock, P. Lightfoot, C. Ritter, J. Solid State Chem. 149 (2000) 92–98.
[22] J. Wang, B.H. Toby, P.L. Lee, L. Ribaud, S.M. Antao, C. Kurtz, M. Ramanathan, R.B. Von Dreele, M.A. Beno, Rev. Sci. Instrum. 79 (2008) 7.
[23] P.L. Lee, D. Shu, M. Ramanathan, C. Preissner, J. Wang, M.A. Beno, R.B. Von Dreele, L. Ribaud, C. Kurtz, S.M. Antao, X. Jiao, B.H. Toby, J. Synchrotron Radiat. 15 (2008) 427–432.
[24] A.C. Larson, R.B. Von Dreele, GSAS—general structure analysis system, Report LA-UR-86-748, Los Alamos Laboratory, 1987.
[25] B.H. Toby, J. Appl. Crystallogr. 34 (2001) 210–213.
[26] H.M. Rietveld, J. Appl. Crystallogr. 2 (1969) 65–71.
[27] G.W. Stinton, J.S.O. Evans, J. Appl. Crystallogr. 40 (2007) 87–95.
[28] D. Taylor, Br. Ceram. Trans. J. 83 (1984) 92–98.
[29] A.P. Hammersley, S.O. Svensson, M. Hanfland, A.N. Fitch, D. Hausermann, High Pressure Res. 14 (1996) 235–248.
[30] P.M. Forster, A. Yokochi, A.W. Sleight, J. Solid State Chem. 140 (1998) 157–158.
[31] M. Cetinkol, A.P. Wilkinson, Solid State Commun. 149 (2009) 421–424.
[32] R.D. Shannon, Acta Crystallogr. A 32 (1976) 751–767.